ACS APPLIED MATERIALS & INTERFACES

Research Article

www.acsami.org

Facile Synthesis of Hierarchically Structured Magnetic $MnO_2/ZnFe_2O_4$ Hybrid Materials and Their Performance in Heterogeneous Activation of Peroxymonosulfate

Yuxian Wang, Hongqi Sun,* Ha Ming Ang, Moses O. Tadé, and Shaobin Wang*

Department of Chemical Engineering and CRC for Contamination Assessment and Remediation of the Environment (CRC CARE), Curtin University, GPO Box U1987, Perth, Western Australia 6845, Australia

Supporting Information

ABSTRACT: In heterogeneous catalysis for water treatment, feasible recovery of nanocatalysts is crucial to make the process cost-effective and environmentally benign. In this study, we applied two strategies, for example, magnetic separation and hierarchical structure of solid catalysts, to ensure manganese catalysts are readily separable, meanwhile their catalytic performance was retained by the nanosized structure of MnO_2 nanosheets or nanorods. $ZnFe_2O_4$ was used as the magnetic core and MnO_2 corolla-like sphere consisting of nanosheets, and sea-urchin shaped structure made of nanorods, were fabricated by a hydrothermal method at 100 and 140 °C, respectively. Crystalline structure, morphology and textural property of the materials were investigated. The prepared catalysts were able to effectively activate peroxymonosulfate (PMS) to generate sulfate radicals for catalytic oxidation of a typical organic pollutant of phenol. After the heterogeneous catalysis, the catalysts were easily recovered by applying an external magnetic field. The effects of temperature and repeated use on the degradation efficiencies were evaluated. The generation and evolution of sulfate radicals and phenol oxidation were studied using both competitive radical tests and electron paramagnetic resonance (EPR).

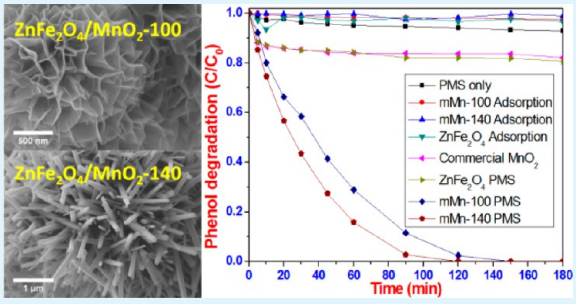

KEYWORDS: *heterogeneous catalysis, magnetic catalysts, manganese oxide, oxone, phenol*

1. INTRODUCTION

Wastewater from processing industries contains many hazardous organics, such as phenolic compounds and dyes, which are highly toxic and recalcitrant to natural degradation and have caused serious issues to the environment.[1,2] Intensive research interests have been focused on complete degradation of these hazardous organics for water reuse. In the past few years, advanced oxidation processes (AOPs), such as catalytic ozonation, wet air oxidation, Fenton and Fenton-like reactions, and photocatalysis have gained increasing attention due to the high efficiency, complete decomposition of organics and almost nonselective degradation.[3] Among these AOPs, Fenton reaction is most popular and has been widely used. Hydroxyl radicals, generated from Fenton/Fenton-like reactions employing H_2O_2 as the oxidant, are the main reactive radicals responsible for oxidation reactions.[4,5] However, utilizing hydroxyl radicals suffers from several drawbacks such as metal leaching, pH adjustment, difficulties in transportation and storage of H_2O_2, and cost-intensive sludge processing and disposal.[6]

Recently, sulfate radicals generated from peroxymonosulfate (oxone, PMS) or persulfate (PS) have been applied as an alternative to hydroxyl radicals. Previous investigations have indicated that sulfate radicals are more reactive than hydroxyl radicals due to a higher redox potential (E_0 = 3.1 V vs E_0 = 2.7 V) and is more selective for oxidation.[7,8] Compared with H_2O_2, the employment of PMS or PS as the initiators for producing sulfate radicals is not only cost-effective because of no pH adjustment, but also more environmentally benign.[9] Many studies have shown that transition metals, especially cobalt ions or oxides, are the best catalysts for PMS activation.[10,11] However, being as a toxic heavy metal, the presence of cobalt in reaction solutions could cause serious health problems.[12,13] For a feasible application, it is urgent to develop novel and recoverable catalysts to minimize the heavy metal leaching while maintaining a high activity in heterogeneous PMS activation.

More recently, manganese-based materials have been widely developed for applications of catalysis, energy storage and conversion because of their superior physical and chemical properties.[14−17] As a catalyst, they not only possess a great potential because of the unique Mn^{2+}/Mn^{4+} redox loop involving a single electron transfer,[18] but also are less toxic than cobalt to the environment. Synthesis of hierarchically structured three-dimensional (3D) manganese materials would be of more interests because they possess both the properties of bulk materials and nanostructure. Recently, 3D α-Mn_2O_3

Received: August 11, 2014
Accepted: October 28, 2014
Published: October 28, 2014

micromaterials in different shapes were prepared and their catalytic activities with PMS for phenol decomposition were tested. It was found that α-Mn_2O_3 cube presented the best catalytic activity than octahedral and truncated octahedral α-Mn_2O_3.[18] Because of the intrinsic arrangement of the atoms on the exposed facets, the catalytic activity of shape-controlled materials can be improved.[19]

For catalyst recycling, magnetic separation technology using external magnetic fields provides a convenient and cost-effective way.[20,21] Over the past decades, magnetite (Fe_3O_4) nanoparticles have been widely used in drug delivery[22−24] and catalyst separation.[25,26] The magnetic nanoparticles suffer from the drawbacks, such as strong dipole−dipole attraction between particles and susceptible to oxidation when exposing to the atmosphere.[27] $ZnFe_2O_4$ nanoparticles have been proposed as an alternative because of their better dispersion and outstanding stability in water and atmosphere.[28,29] Apart from being a magnetic material,[30] $ZnFe_2O_4$ nanoparticles have successfully demonstrated their extensive applications in photocatalysis,[31] adsorption,[32] and solar cells.[33,34] Compared with other magnetic materials, $ZnFe_2O_4$ possesses advantages of high stability under humid air, easy synthesis, and low cost.[35,36] $ZnFe_2O_4$ also shows better dispersion and less dipole−dipole attraction than iron-based magnetic materials.[29]

To the best our knowledge, no studies have been reported on synthesis of magnetic 3D-hierarchically structured $ZnFe_2O_4$/MnO_2 hybrid structures. In this study, we first demonstrated a facile hydrothermal method to synthesize magnetically separable MnO_2 by hydrothermal treatment of $KMnO_4$ with HCl, in which $ZnFe_2O_4$ was used as the magnetic dots integrated on the MnO_2 substructure. 3D hierarchical structures were able to be selectively obtained by simply varying the hydrothermal reaction temperature. The prepared catalysts showed outstanding catalytic activity in activation of PMS for degradation of phenol solutions, and the activation mechanism was also studies using competitive radical tests and electron paramagnetic resonance (EPR) analysis.

2. EXPERIMENTAL SECTION

2.1. Materials. Potassium permanganate (99.8%), hydrochloric acid (37%), iron(III) chloride hexahydrate (99.8%), zinc chloride (99.5%), and 5,5-dimethyl-1-pyrroline (DMPO, >99.0%) were purchased from Sigma-Aldrich. Oxone ($2KHSO_5{\cdot}KHSO_4{\cdot}K_2SO_4$, PMS) was obtained from Aldrich. Phenol (99.0%) was purchased from AJAX. Sodium acetate (99.5%), ethylene glycol (99.0%) and commercial activated Mn (IV) dioxide (99.9%) were obtained from Fluka. All chemicals were used as received without any further purification.

2.2. Synthesis of $ZnFe_2O_4$/MnO_2 Hybrid Structures. $ZnFe_2O_4$ nanoparticles were synthesized via a modified hydrothermal method, which is shown in Supporting Information (SI). For synthesis of $ZnFe_2O_4$/MnO_2 hybrid structures, 0.25 g of $ZnFe_2O_4$ was dispersed in 80 mL of ultrapure water by sonication for 10 min. Then 0.45 g $KMnO_4$ and 1 mL of 37% HCl were added to the suspension under vigorous stirring. After it was stirred for about 30 min, the homogeneous solution was transferred into a Teflon-lined stainless steel autoclave with the capacity of 120 mL. The autoclave was tightly sealed and heated in an electric oven at 100 and 140 °C for 12 h, respectively. After the autoclave was naturally cooled down to room temperature, each of the black precipitate was harvested by vacuum filtration and washed with deionized water 3 times before being dried at 60 °C overnight. According to the hydrothermal temperature, the obtained samples were labeled as mMn-100 and mMn-140, respectively. According to the recovery, the weight loading of MnO_2 was calculated to be 50.5% and 59.2% for mMn-100 and mMn-140, respectively.

2.3. Characterization. Powder X-ray diffraction (XRD) patterns of samples were determined on a Bruker D8 X-ray diffractometer (Bruker-AXS, Karlsruhe, Germany) with filtered Cu Kα radiation (λ = 1.5418 Å), at accelerating voltage and current of 40 kV and 40 mA, respectively. The structure and morphology of samples were observed on a field emission scanning electron microscope (FESEM, ZEISS NEON 40EsB). Transmission electron microscopy (TEM) was operated on a JEOL 2011 TEM instrument. The surface area and pore size distribution of samples were evaluated by N_2 adsorption/desorption at −196 °C using a Micromeritics Tristar 3000. The Brunauer−Emmett−Teller (BET) specific surface area was obtained by applying the BET equation. The pore size distribution was obtained by the Barret−Joyner−Halenda (BJH) method.

2.4. PMS Activation and Catalytic Oxidation. To evaluate the activity of catalysts in oxidation of phenol, batch experiments were carried out in a 500 mL reactor containing 20 ppm phenol solution. The reactor was attached to a stand and dipped into a water bath with a temperature controller. Unless specifically stated, the reaction temperature was 25 °C. In a typical test, 0.1 g of catalyst was first added to the phenol solution, and the mixture was kept stirring at a constant speed of 400 rpm. After adsorption−desorption equilibrium on the catalyst was achieved, 1 g of oxone was added to start the reaction. At predetermined time intervals, 1 mL of liquid was withdrawn from the reaction solution using a syringe and filtered into a high performance liquid chromatography (HPLC) vial, and 0.5 mL of methanol was added to quench to reaction. The concentrations of withdrawn phenol samples were analyzed using a Varian HPLC with a UV detector set at a wavelength of 270 nm. The C-18 HPLC column was used to separate the organics and the mobile phase was made of 30% CH_3CN and 70% water with a flow rate of 1 mL/min. For the recycle tests of the catalyst, the solid material was obtained by filtration and washed with ultrapure water for several times after each run. Then the washed catalyst was dried in an oven at 60 °C for 12 h. Electron paramagnetic resonance (EPR) experiments were performed on a Bruker EMX-E spectrometer (Germany) with DMPO as a spin-trapping agent for radical measurement.

3. RESULTS AND DISCUSSION

3.1. Characterization of the Hierarchical Materials. The crystalline structures of samples were investigated by XRD. The XRD pattern of the as-prepared $ZnFe_2O_4$ is shown in Figure 1A. As seen, the diffraction peaks found at 2θ of 30.2, 35.5, 42.9, 53.3, 56.8, and 62.3° confirm the formation of cubic $ZnFe_2O_4$ with a spinel structure (JCPDS No. 77-0011).[28] And these peaks can be indexed to (220), (311), (400), (422), (511), and (440) planes of spinel $ZnFe_2O_4$, respectively. The average crystallite size of $ZnFe_2O_4$ was estimated to be 19.4 nm by the Debye−Scherrer formula. Figure 1B presents the XRD patterns of $ZnFe_2O_4$/MnO_2 hybrid structures synthesized at 100 and 140 °C, respectively. Characteristic diffraction peaks of $ZnFe_2O_4$ were observed on both $ZnFe_2O_4$/MnO_2 samples, indicating the presence of $ZnFe_2O_4$ in these samples. For $ZnFe_2O_4$/MnO_2 synthesized at 100 °C, peaks at 12.3°, 25.5°, 36.7°, and 66.2° were also observed, corresponding to a pure layered birnessite-type MnO_2 (JCPDS No. 80−1098, monoclinic, C2/*m*, *a* = 5.15 Å, *b* = 2.84 Å, *c* = 7.17 Å), denoted as δ-MnO_2.[15] And the diffraction peaks identified correspond to the crystal planes of (0 0 1), (0 0 2), (1 1 1), and (3 1 1), respectively. When hydrothermal temperature was elevated to 140 °C, according to the corresponding diffraction peaks, the manganese oxide was found to be pure α-MnO_2 (JCPDS No. 44-0141, tetragonal, I4/*m*, *a*=*b* = 9.78 Å, *c* = 2.86 Å).[17] In this temperature-elevation process, the crystalline structure of MnO_2 experienced a transformation from δ-type to α-type,

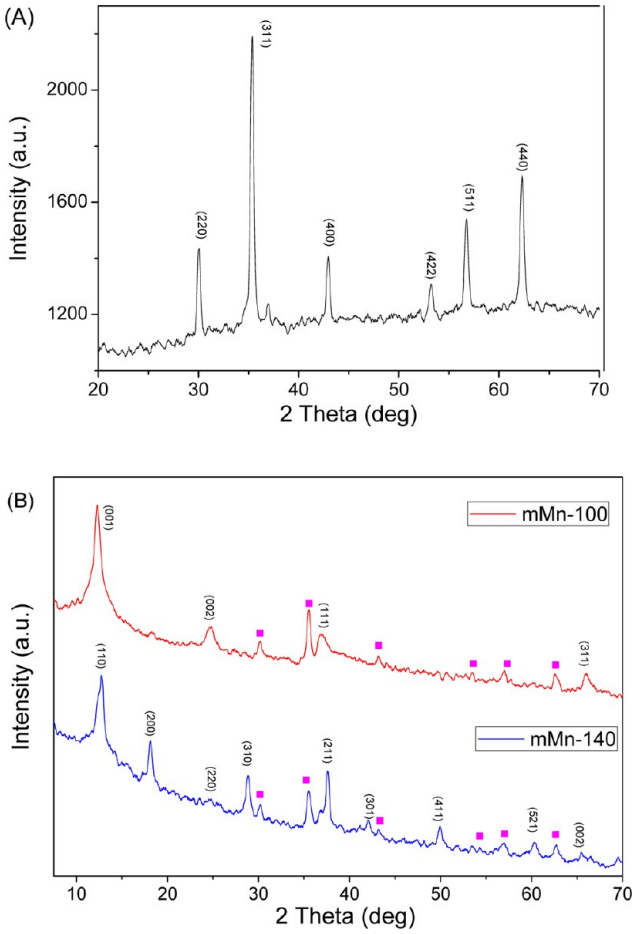

Figure 1. XRD patterns of $ZnFe_2O_4$ (A) and mMn-100 and mMn-140 (B). pink box, $ZnFe_2O_4$ peaks.

revealing temperature-dependent property of MnO_2 structure. Since no other characteristic peaks from impurities were observed, the obtained samples were confirmed to be of high purity.

The reactions involved during the hydrothermal processes can be briefly described as follows:[37]

$$2KMnO_4 + 8HCl \xrightarrow{100\ ^\circ C} 2MnO_2(\delta\ \text{type}) + 3Cl_2 + 2KCl + 4H_2O \quad (1)$$

$$2KMnO_4 + 8HCl \xrightarrow{140\ ^\circ C} 2MnO_2(\alpha\ \text{type}) + 3Cl_2 + 2KCl + 4H_2O \quad (2)$$

Structure and morphology of the magnetic catalysts are displayed by SEM images. Figure S1 (Supporting Information) illustrates SEM image of $ZnFe_2O_4$ nanoparticles. It was found that these nanoparticles agglomerated and presented a sphere-like morphology with the average size of 10−20 nm, which is well in agreement with XRD result. The agglomeration of these nanoparticles can be ascribed to the magnetic dipole interaction between them and the high surface energy because of their nanoscaled size.[38] Figure 2A and B show SEM images of mMn-100, the sample prepared at 100 °C. It can be observed that this sample shows a uniform corolla-like structure consisting of microsphere/nanosheet hierarchical nanostructures with an average diameter around 2 μm. The crystal growth processes of this hierarchical structure include several stages. In the initial stage, a large number of nuclei were formed by the reactions of $KMnO_4$ and HCl solution.[15] Due to the high surface energy, these nuclei were captured by the well dispersed $ZnFe_2O_4$ nanoparticles and then grew on their surfaces to encapsulate the $ZnFe_2O_4$ and form sphere-like structure. At last, the heterogeneous growth of 2D nanosheets on these nuclei happened following a general Ostwald ripening process.[39,40]

When the hydrothermal temperature was increased to 140 °C, tetragonal α-MnO_2 was produced. As a result, the morphology of mMn-140 transformed to hierarchical sea-urchin shaped microstructure with a diameter of 3−4 μm, made of straight tetragonal nanorods with a uniform diameter of 30−40 nm (Figure 2C and D). The transformation of MnO_2 crystalline structure from layered δ-phase to tetragonal α-phase can be assigned to anisotropic growth of crystal favored at elevated temperature to provide higher aspect ratios.[41]

Figure 3 shows TEM images for mMn-100 and mMn-140. On mMn-100, a two-dimensional sheet-like structure consisting of wrinkles was observed, suggesting a sub-block of 2D layer from the 3D corona-like spheres. Magnetic $ZnFe_2O_4$ nanoparticles were attached on the layers. For mMn-14, $ZnFe_2O_4$ nanoparticles were found to be distributed on the surface of the 1D nanorods of the 3D urchin-like structure. The $ZnFe_2O_4$ nanoparticles in both samples were dispersed well on the MnO_2. Moreover, the $ZnFe_2O_4$ nanoparticles had an average size around 10−20 nm, which was in agreement with the average particle size calculated using the Schererr's formula based on XRD patterns.

N_2 sorption isotherms and pore size distributions of $ZnFe_2O_4/MnO_2$ samples were evaluated through N_2 adsorption/desorption measurements (Figure 4). According to the IUPAC classification, both of the samples presented a type IV isotherm with a type H3 hysteresis loop, indicating a typical mesoporous structure.[42] As seen, the samples displayed a broad hysteresis loop at a relative pressure range (P/P_0) of 0.4 to 0.95. However, the hysteresis loop on mMn-100 was broader than that of mMn-140, suggesting a more porous structure and thus larger surface area and pore volume, which were confirmed by the results shown in Table 1. The BET specific surface area of mMn-100 is about 50% greater than that of mMn-140 (166.5 vs 113.1 m^2/g), which might be owing to the vast spaces between 2D layered hierarchical structures grown on the surfaces. While the pore size distributions for both samples are quite similar: a single modal pore diameter distribution centered at around 2.5 nm was observed for each sample.

3.2. Catalytic Oxidation of Phenol. Figure 5 shows the adsorption and phenol degradation profiles on various samples. To compare the catalytic activity of the samples, control experiments were carried out to evaluate phenol removal caused by catalyst adsorption and PMS self-activation at ambient environment. As seen, less than 10% phenol was degraded when PMS was alone involved in the reaction without a catalyst, indicating that PMS could not be effectively activated under ambient thermal condition. For adsorption tests, both $ZnFe_2O_4/MnO_2$ samples exerted insignificant phenol removal, suggesting that phenol removal by adsorption was negligible during the heterogeneous catalytic reaction. The fluctuation of phenol removal profiles in adsorption tests might be ascribed to that samples were achieving adsorption/desorption equilibrium.

For catalytic reactions, $ZnFe_2O_4$ was tested with PMS first and it showed a noncompetitive catalytic activity. Around 20% phenol was degraded within 180 min. A commercial MnO_2 sample provided a similar efficiency, less than 20% of phenol

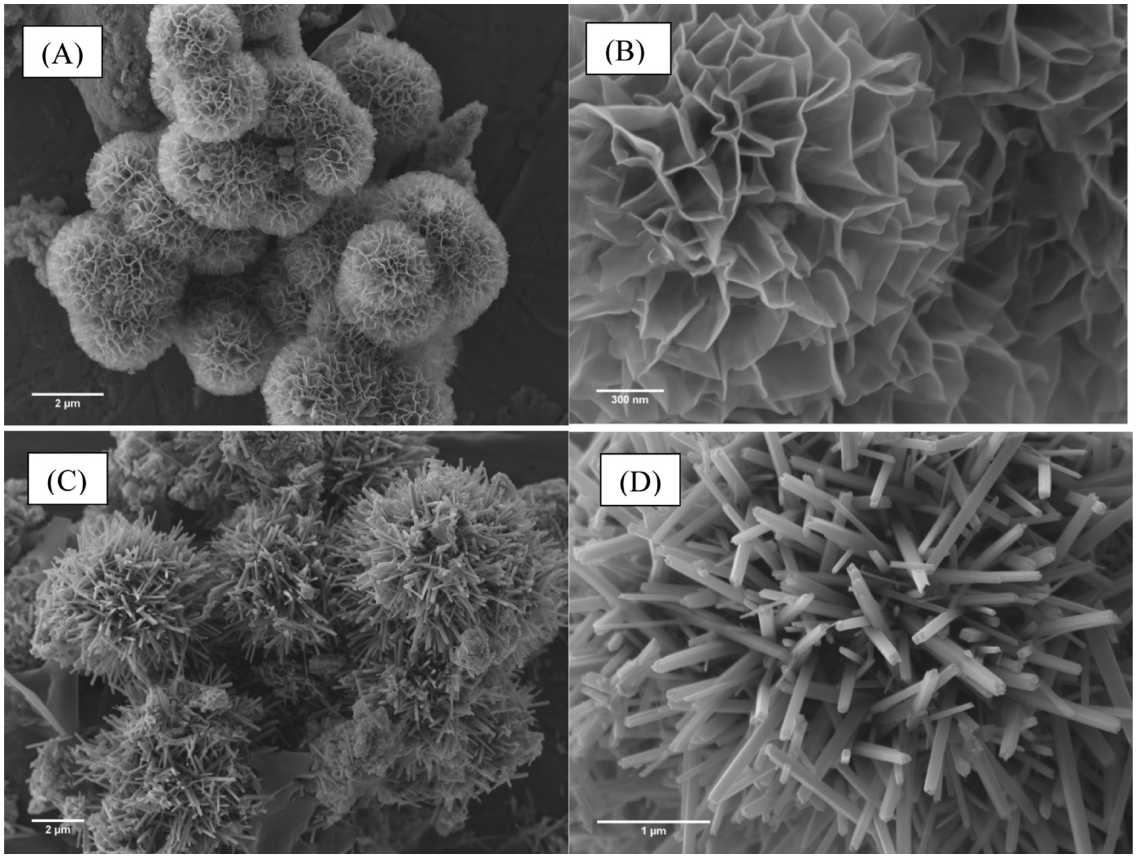

Figure 2. SEM images of $ZnFe_2O_4/MnO_2$ samples. (A) and (B) mMn-100, (C) and (D) mMn-140.

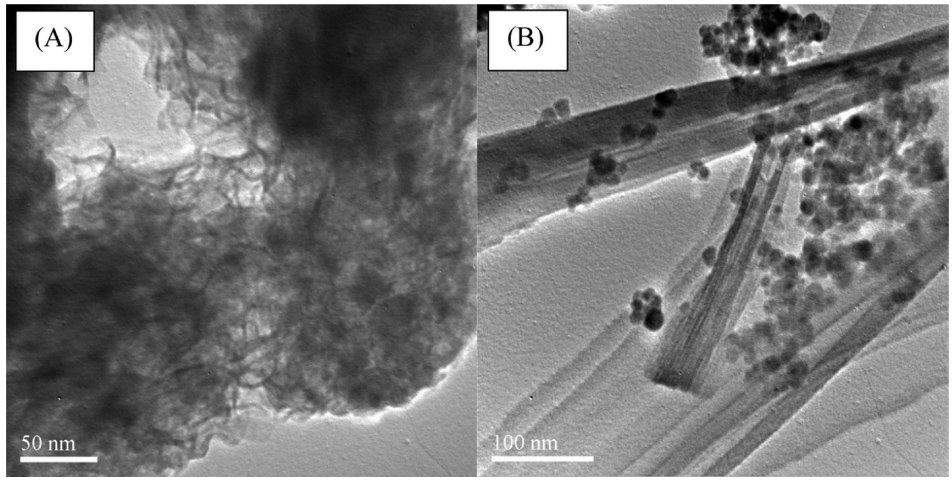

Figure 3. TEM images of (A) mMn-100 and (B) mMn-140.

was degraded after 180 min. However, mMn-100 demonstrated a much better catalytic activity, and 100% removal of phenol was achieved within 120 min while the catalytic activity of mMn-140 was slightly lower providing 100% phenol degradation within 150 min. It was found that the activities followed the order of their BET specific surface area, indicating that higher surface area would provide more active sites for catalytic reaction.

For reaction kinetic studies, a first-order mode (eq 3) was employed to evaluate the catalytic reaction kinetics

$$\ln\left(\frac{C}{C_0}\right) = -kt \tag{3}$$

where C is the concentration of phenol at time t, C_0 is initial phenol concentration, and k is the first-order reaction rate constant. Figure S2 (Supporting Information) shows that phenol degradation curve was well fitted with the first-order kinetics with high values of regressions coefficients. The reaction rate constants for the two catalysts are provided in Table 1.

The as-synthesized $ZnFe_2O_4/MnO_2$ catalysts can be easily recycled from reaction solution by simply applying an external

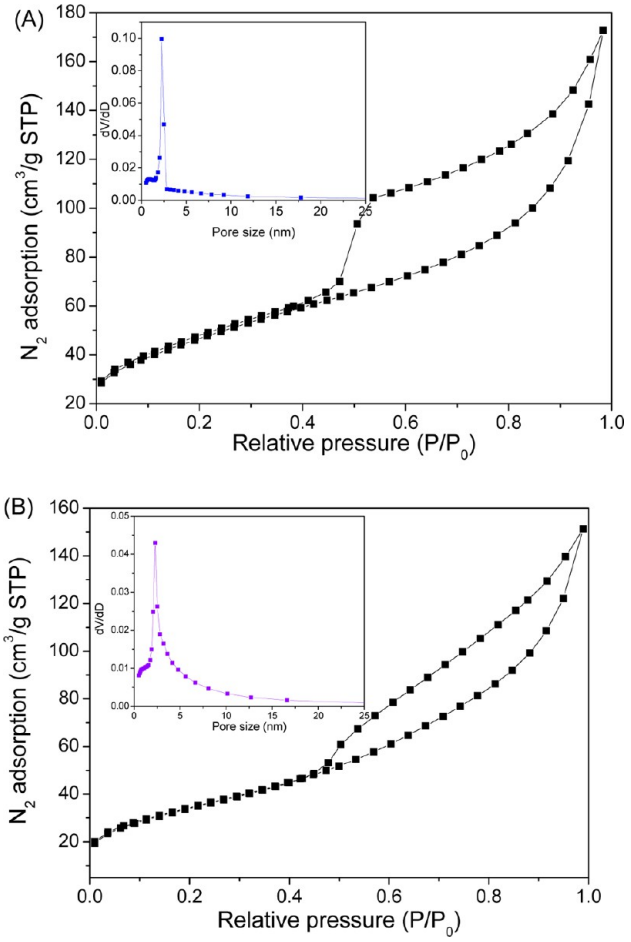

Figure 4. Nitrogen sorption isotherms and pore size distributions of (A) mMn-100 and (B) mMn-140.

Table 1. Textural Properties of Supported MnO_2 and Their Activities in Phenol Degradation

catalyst	surface area (S_{BET}, m^2/g)	pore volume (cm^3/g)	first-order rate constant (min^{-1})	R^2
mMn-100	166.5	0.161	0.032	0.998
mMn-140	113.1	0.154	0.022	0.997

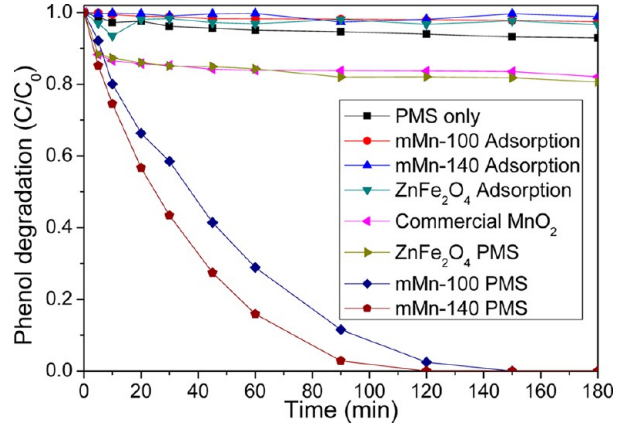

Figure 5. Phenol removal in various conditions. Reaction conditions: $[phenol]_0$ = 20 mg/L, catalyst loading = 0.2 g/L, oxone loading = 2.0 g/L, temperature = 25 °C.

magnetic field. As shown in Figure S3 (Supporting Information), both of the $ZnFe_2O_4/MnO_2$ catalysts can be well dispersed in deionized water and form a stable suspension before magnetic separation (Supporting Information Figure S3A). When a magnet was approached to the glass vial, both of the samples rapidly accumulated to the magnet side, and nearly transparent solution was obtained within 3 min (Supporting Information Figure S3B). Removing the external magnetic field and sonicating the solution, the solid samples can be dispersed again in solution. Since attraction and dispersion processes can be readily altered by simply approaching or removing an external magnetic field, the as-synthesized $ZnFe_2O_4/MnO_2$ catalysts demonstrated excellent water dispersion and magnetic attraction for effective separation.[16]

Reaction temperature is a key operating factor in AOPs. Phenol degradation was examined within a temperature range of 25 to 45 °C for both $ZnFe_2O_4/MnO_2$ catalysts by heterogeneous activation of PMS, and the results are shown in Figure 6. A general trend observed for both catalysts is that

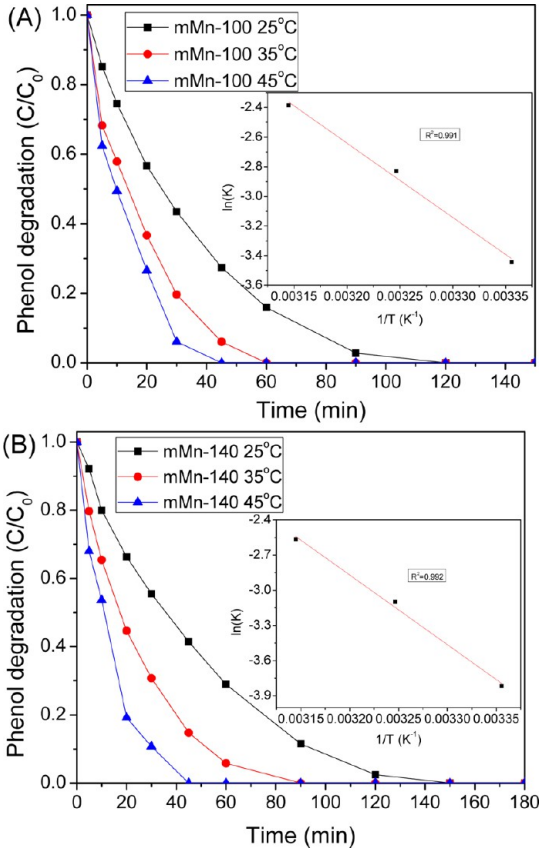

Figure 6. Effect of reaction temperature on phenol degradation and estimation of activation energy for (A) mMn-100 and (B) mMn-140. Reaction conditions: $[phenol]_0$ = 20 mg/L, catalyst loading = 0.2 g/L, oxone loading = 2.0 g/L.

temperature will remarkably influence the reaction rate, higher temperature resulting in higher reaction rate. As seen, for mMn-100, when temperature was enhanced from 25 to 45 °C, the time for 100% phenol degradation decreased dramatically from 120 to 45 min. Meanwhile similar phenol degradation profiles were also observed for mMn-140. On the basis of this trend, it might be deduced that PMS activation process is endothermic: higher temperature would shift the equilibrium to produce

more reactive species and thus improve the phenol degradation efficiency.

All of these reaction profiles were then fitted with the first order kinetics, and the kinetic rate constants are presented in Table 2. The rate constants (K) at varying temperatures for

Table 2. Kinetic results of $ZnFe_2O_4/MnO_2$ Catalysts in Activation of PMS for Phenol Degradation at Different Temperatures

catalyst	T (°C)	k (min^{-1})	R^2 of k	E_a (kJ/mol)	R^2 of E_a
mMn-100	25	0.032	0.991	41.7	0.991
	35	0.059	0.989		
	45	0.092	0.999		
mMn-140	25	0.022	0.994	49.4	0.992
	35	0.045	0.994		
	45	0.077	0.989		

mMn-100 were higher than those of mMn-140, which was in accordance with the degradation profiles in Figure 6. By plotting the ln K against $1/T$ (insets of Figure 6A and B) based on the Arrhenius equation, activation energies (E_a) of the catalytic reaction for mMn-100 and mMn-140 can be calculated as 41.7 and 49.4 kJ/mol, respectively. And the lower activation energy of mMn-100 validated its higher catalytic activity than mMn-140. The lower activation energy of mMn-100 might be due to the different crystal structure and preferential facet. When comparing with standard XRD patterns, it was found that mMn-100 had δ-phase with a main exposure of (001), while mMn-140 had α-phase with (110) as main facet. The different crystal phase and facet will contribute to the lower activation energy and higher catalytic performance of mMn-100.

To our best knowledge, no investigation has been reported on supported MnO_2 or magnetic MnO_2 hybrid structure for activation of PMS for phenol degradation. However, a few studies have been carried out using Mn-based catalysts for heterogeneous activation of PMS for organic removal. Table 3

Table 3. Comparison of Activation Energy of Mn-Based Catalysts

catalyst	organics	E_a (kJ/mol)	ref
Mn_3O_4-rGO	orange II	49.5	9
$MnFe_2O_4$	orange II	31.7	43
$MnFe_2O_4$-rGO	orange II	25.7	43
Co_3O_4/MnO_2	phenol	20.3	44
α-MnO_2 nanowire	phenol	21.9	14
$ZnFe_2O_4/MnO_2$-100	phenol	41.7	this study
$ZnFe_2O_4/MnO_2$-140	phenol	49.4	this study

presents the activation energies obtained from these investigations on PMS activation using the as-mentioned catalysts. It was found that magnetic MnO_2 catalysts in this study had higher activation energies in phenol oxidation.

The stability and recyclability of $ZnFe_2O_4/MnO_2$ catalysts were also evaluated by successive three-run reusability tests (Figure 7). The catalysts were treated by simple water washing without any further regeneration. A general trend for both catalysts is that catalytic activities decreased in recycled tests. As seen in the third run, for both catalysts, 20% of phenol still remained in solution at the end of each reaction, indicating the deactivation of the catalysts. The decrease in catalytic activity

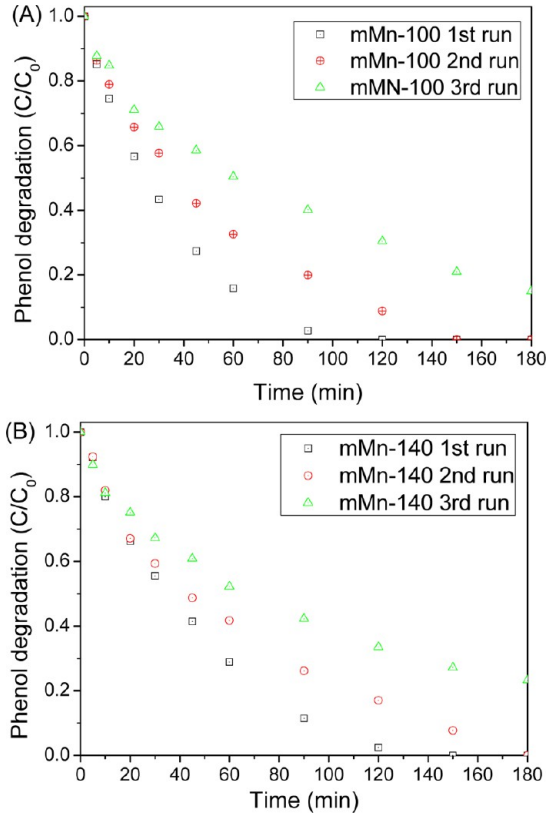

Figure 7. Phenol degradation on mMn-100 and mMn-140 at different runs after repeated uses. (A) Phenol degradation on mMn-100 at different runs after repeated uses. (B) Phenol degradation on mMn-140 at different runs after repeated uses. Reaction conditions: $[phenol]_0$ = 20 mg/L, catalyst loading = 0.2 g/L, oxone loading = 2.0 g/L, and T = 25 °C.

might be attributed to the attachment of reaction intermediates on the catalyst surface, which thus deactivated the correspondent active sites. Because of the strong Van de Waals force, these intermediates cannot be fully removed by simple water washing. Recently, we have reported that deactivation induced by attachment of intermediates can be eliminated by calcination at high temperature either in air or N_2 atmosphere.[25,45]

3.3. Activation Processes of PMS and Mechanism of Phenol Degradation. Previous studies have reported that PMS can generate hydroxyl radicals ($^{\bullet}OH$) and sulfate radicals ($SO_4^{\bullet-}$) by either homogeneous or heterogeneous activation for phenol degradation.[46,47] Peroxymonosulfate radicals ($SO_5^{\bullet-}$) might be also formed, but would not contribute to phenol degradation due to the low redox potential.[48] To detect the reactive species generated during the PMS activation process, electron paramagnetic resonance (EPR) tests with DMPO as the spin trapping agent were conducted.

Control experiments were conducted to investigate PMS self-activation without the presence of catalysts. As seen in Figure S4 (Supporting Information), when 2 g/L PMS solution was tested without addition of phenol, characteristic signals of 5,5-dimethylpyrroline-(2)-oxyl-(1) (DMPOX), the nitroxide radical of DMPO, were observed.[49] The occurrence of DMPOX signals can be ascribed to the immense amount of hydroxyl radicals produced by strong hydrolysis process of HSO_5^-, which directly oxidized DMPO to DMPOX without the presence of phenol.[50] The relevant hydrolysis reactions of HSO_5^- are shown in eqs 4 and 5.

$$HSO_5^- + H_2O \leftrightarrow H_2O_2 + HSO_4^- \quad (4)$$

$$H_2O_2 \rightarrow {}^{\bullet}OH + {}^{\bullet}OH \quad (5)$$

When 20 ppm of phenol was added in solution without any catalyst, it could be observed that characteristic peaks of DMPO-HO$^{\bullet}$ adducts having the intensity ratio of 1:2:2:1 (with hyperfine splitting constants of $a_N = a_H = 14.9$ G) were presented, indicating that hydroxyl radicals were produced with the presence of phenol.[51] The absence of DMPOX peaks revealed that hydroxyl radicals prefer to react with phenol rather than DMPO.[52]

Figure 8A and B display EPR spectra of reactive radicals generated during the catalytic oxidation on $ZnFe_2O_4/MnO_2$ with PMS (2 g/L) for phenol (20 mg/L) degradation. As seen, EPR spectra for both catalysts show the identical trend. Within the overall activation and oxidation processes, both $^{\bullet}OH$ and $SO_4^{-\bullet}$ were produced through the identification of signals of DMPO-HO$^{\bullet}$ and DMPO−$SO_4^{-\bullet}$ adducts, respectively. At the beginning of the reaction (1 min), only hydroxyl radicals were produced by identification of DMPO-HO$^{\bullet}$ adducts, which was similar to that of PMS reacting with phenol solution without the presence of catalysts. This similarity indicates that at the very initial stage of the reaction, the peroxymonosulfate anions (HSO_5^-) were not fully bonded with the active sites on the catalyst surface to be activated to generate sulfate radicals.

When reaction time was prolonged to 5 min, besides the presence of signals of DMPO-HO$^{\bullet}$ adducts, signals of DMPO−$SO_4^{\bullet-}$ adducts (with hyperfine splitting constants of $a_N = 13.2$ G, $a_H = 9.6$ G, $a_H = 1.48$ G, and $a_H = 0.78$ G)[51] were also detected, suggesting that HSO_5^- had been activated to produce sulfate radicals at this reaction stage. In addition, the appearance of $SO_4^{\bullet-}$ led to the decrease of DMPO-HO$^{\bullet}$ signal intensity, which indicates that, in the presence of catalysts, hydroxyl radicals could induce the generation of sulfate radicals. When reaction time was further extended to 10 min, the signal intensity of DMPO−$SO_4^{\bullet-}$ adducts increased, indicating more sulfate radicals had been produced compared with the reaction at 5 min. However, at 30 min, little or no intensities of DMPO−$SO_4^{\bullet-}$ adducts could be detected, suggesting the depletion of sulfate radicals by the rapid reaction, and only signals of DMPO-HO$^{\bullet}$ adducts remained, which was again similar to the initial condition. On the basis of this appearance/disappearance cycle of sulfate radicals and the phenol degradation profiles shown in Figure 5, it can be deduced that sulfate radicals are more active than hydroxyl radicals in phenol degradation process and are responsible for phenol degradation.

Figure 8C shows the evolution of the peak intensities of DMPO−$SO_4^{\bullet-}$ adducts dependence on time over both $ZnFe_2O_4/MnO_2$ catalysts. As shown clearly, the peak intensities for DMPO−$SO_4^{\bullet-}$ adducts displayed a cycle-like trend. Moreover, the DMPO−$SO_4^{\bullet-}$ peak intensities for mMn-100 were generally higher than those of mMn-140, suggesting that amount of sulfate radicals produced by mMn-100 were greater than those of mMn-140 and thus mMn-100 showed a higher catalytic activity. This observation was not only in accordance with the phenol degradation (shown in Figure 5), but also further confirmed the importance of sulfate radicals in phenol degradation.

To further investigate the major reactive radical species responsible for phenol degradation, competitive radical tests using ethanol (EtOH) and *tert*-butyl alcohol (TBA) as

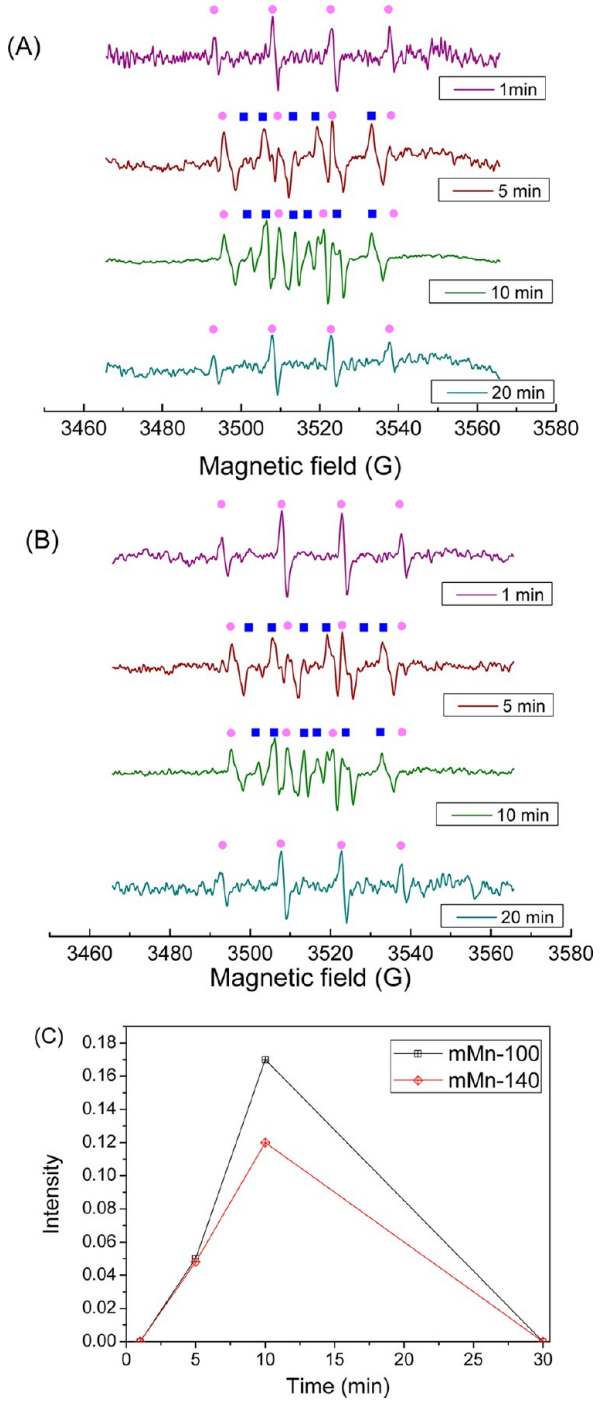

Figure 8. EPR spectra in various conditions. (A) Reactive radical dependence on activation time over mMn-100, (B) reactive radical dependence on activation time over mMn-140, (C) comparison of sulfate radicals on mMn-100 and mMn-140. Centerfield: 3517 G. Sweep width: 100 G. Microwave frequency: 9.87 GHz. Modulation frequency: 100 GHz. Power: 18.11 mW. Reaction conditions: $[phenol]_0$ = 20 mg/L, catalyst loading = 0.2 g/L, oxone loading = 2.0 g/L, pH = 7.0, DMPO = 0.08 M. pink circle, DMPO-HO$^{\bullet}$; blue box, DMPO−$SO_4^{\bullet-}$.

quenching agents were also carried out. Researches have shown that both EtOH and TBA could sufficiently quench $^{\bullet}OH$ and the reaction rates are nearly diffusion controlled at $1.2 \times 10^9 - 2.8 \times 10^9$ and $3.8 \times 10^8 - 7.6 \times 10^8$ M^{-1} s^{-1}, respectively.[53] While $SO_4^{\bullet-}$ is selective to be quenched more

rapidly by EtOH with α-hydrogen than TBA without α-hydrogen (1.6×10^7–7.7×10^7 M^{-1} s^{-1} vs 4.0×10^5–9.1×10^5 M^{-1} s^{-1}).[48,53] Therefore, by addition of EtOH or TBA into reaction solution, the responsible radical species for phenol degradation could be well differentiated.

Figure 9 shows the changes of phenol degradation in form of reaction rate constant k. Both $ZnFe_2O_4/MnO_2$ catalysts shared

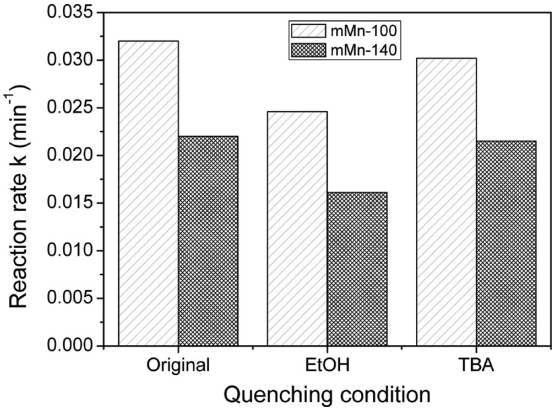

Figure 9. Changes of reaction rate (k) of $ZnFe_2O_4/MnO_2$ catalysts with and without quenching agents of EtOH (0.2 M) and TBA (0.2 M). Reaction conditions: $[phenol]_0$ = 20 mg/L, catalyst loading = 0.2 g/L, oxone loading = 2.0 g/L, and T = 25 °C.

a similar trend; when 0.2 M EtOH was added in the original reaction solution, remarkable decrease in reaction rate was observed, suggesting that part of the hydroxyl and sulfate radicals were quenched. However, by addition of 0.2 M TBA, negligible decrease occurred to the reaction rate, indicating that, with the quenching of hydroxyl radicals, sulfate radicals could still provide the similar reaction rate. Therefore, the more remarkable decrease of reaction rate caused by EtOH than TBA suggested that the major reactive species dominating phenol degradation were sulfate radicals.

Based on the results of both competitive radical tests and EPR investigations, the mechanism of PMS activation on $ZnFe_2O_4/MnO_2$ for phenol degradation can be proposed as follows:

$$HSO_5^- \rightarrow SO_4^{2-} + {}^{\bullet}OH \quad (6)$$

$${}^{\bullet}OH + Mn(IV) \rightarrow Mn(IV)\text{—}{}^{\bullet}OH \quad (7)$$

$$Mn(IV)\text{—}{}^{\bullet}OH + HSO_5^- \rightarrow Mn(IV)\text{—}{}^{\bullet}OHOSO_3 + OH^- \quad (8)$$

$$Mn(IV)\text{—}{}^{\bullet}OHOSO_3 \rightarrow Mn(III) + {}^{\bullet}OH + SO_4^{\bullet -} \quad (9)$$

$$Mn(III) + HSO_5^- \rightarrow Mn(IV) + SO_5^{\bullet -} + H^+ \quad (10)$$

$$2SO_5^{\bullet -} + 2OH^- \rightarrow 2SO_4^{2-} + 2{}^{\bullet}OH + O_2 \quad (11)$$

$${}^{\bullet}OH + SO_4^{\bullet -} + C_6H_5OH \rightarrow \text{several steps} \rightarrow CO_2 + H_2O + SO_4^{2-} \quad (12)$$

In the first stage, hydrolysis of HSO_5^- happened to produce hydroxyl radicals (eq 6). Then some of the hydroxyl radicals attached on the active sites of MnO_2 based catalysts (eq 7). The Mn(IV) sites with hydroxyl radicals would induce HSO_5^- to produce Mn (IV)—$^{\bullet}OHOSO_3$ and then subsequently to generate sulfate radicals which are dominant for phenol degradation. Meanwhile, some of the attached hydroxyl radicals would also detach (eqs 8 and 9). The produced sulfate radicals and the detached hydroxyl radicals would react with phenol at different reaction rates (eq 12). After the depletion of sulfate radicals, hydroxyl radicals would become the only reactive species for phenol degradation though at an inferior reaction rate. In the meantime, the recovery reaction for the catalyst resulted in the production of the original catalyst, as well as further generation of hydroxyl radicals (eqs 10 and 11). On the basis of the comprehensive investigations, it was suggested that the order of sulfate radicals generation reflects the order of the reaction rates in phenol degradation on the $ZnFe_2O_4/MnO_2$ catalysts.

4. CONCLUSIONS

3-D magnetic $ZnFe_2O_4/MnO_2$ hybrid catalysts with two hierarchical nanostructures were synthesized by a hydrothermal method at varying temperatures. Their catalytic activities were investigated in terms of PMS activation for phenol degradation. It was found that $ZnFe_2O_4/MnO_2$ with microsphere/nanosheet hierarchical structure possessed the higher BET surface area and thus the better catalytic activity than urchin-like catalysts. A first-order kinetic model was used to evaluate the kinetic parameters, and the activation energies for microsphere/nanosheet hierarchical structure and urchin-like structure were calculated to be 41.7 and 49.4 kJ/mol, respectively. Catalyst stability tests suggested that deactivation of the catalysts occurred because of the blockage of active sites by the reaction intermediates. The mechanism of catalytic reaction for activation of PMS was illustrated by competitive radical tests and EPR spectra. Sulfate radicals were the major reactive species taking effect in this catalytic reaction and the generation of sulfate radicals could be induced by hydroxyl radicals produced at the initial stage.

■ ASSOCIATED CONTENT

Supporting Information

Synthesis of $ZnFe_2O_4$, SEM of $ZnFe_2O_4$, first-order kinetic model, magnetic separation and EPR spectra. This material is available free of charge via the Internet at http://pubs.acs.org.

■ AUTHOR INFORMATION

Corresponding Authors

*Tel: +61 8 92669211. Fax: +61 8 92662681. E-mail: h.sun@curtin.edu.au (H.S.).

*Tel:+61 8 92663776. Fax: +61 8 92662681. Email: shaobin.wang@curtin.edu.au (S.W.).

Notes

The authors declare no competing financial interest.

■ ACKNOWLEDGMENTS

The authors acknowledge the use of equipment, scientific and technical assistance of the Curtin University Electron Microscope Facility and Centre for Microscopy Characterization, which has been partially funded by the University, State and Commonwealth Governments. H. S. is grateful for the supports of Curtin Research Fellowship and Opening Project (KL13-02) of State Key Laboratory of Materials-Oriented Chemical Engineering, China.

REFERENCES

(1) Gupta, V. K.; Ali, I.; Saleh, T. A.; Nayak, A.; Agarwal, S. Chemical Treatment Technologies for Waste-Water Recycling—An Overview. *RSC Adv.* **2012**, *2*, 6380−6388.

(2) Gupta, V. K.; Srivastava, S. K.; Tyagi, R. Design Parameters for the Treatment of Phenolic Wastes by Carbon Columns (Obtained from Fertilizer Waste Material). *Water Res.* **2000**, *34*, 1543−1550.

(3) Tušar, N. N.; Maučec, D.; Rangus, M.; Arčon, I.; Mazaj, M.; Cotman, M.; Pintar, A.; Kaučič, V. Manganese Functionalized Silicate Nanoparticles as a Fenton-Type Catalyst for Water Purification by Advanced Oxidation Processes (AOP). *Adv. Funct. Mater.* **2012**, *22*, 820−826.

(4) Wang, S. A Comparative Study of Fenton and Fenton-Like Reaction Kinetics in Decolourisation of Wastewater. *Dyes Pigm.* **2008**, *76*, 714−720.

(5) Watts, R.; Sarasa, J.; Loge, F.; Teel, A. Oxidative and Reductive Pathways in Manganese-Catalyzed Fenton's Reactions. *J. Environ. Eng.* **2005**, *131*, 158−164.

(6) Hu, L.; Yang, X.; Dang, S. An Easily Recyclable Co/SBA-15 Catalyst: Heterogeneous Activation of Peroxymonosulfate for the Degradation of Phenol in Water. *Appl. Catal., B* **2011**, *102*, 19−26.

(7) Tsitonaki, A.; Petri, B.; Crimi, M.; MosbÆK, H.; Siegrist, R. L.; Bjerg, P. L. In Situ Chemical Oxidation of Contaminated Soil and Groundwater Using Persulfate: A Review. *Crit. Rev. Environ. Sci. Technol.* **2010**, *40*, 55−91.

(8) Lente, G.; Kalmár, J.; Baranyai, Z.; Kun, A.; Kék, I.; Bajusz, D.; Takács, M.; Veres, L.; Fábián, I. One- Versus Two-Electron Oxidation with Peroxomonosulfate Ion: Reactions with Iron(II), Vanadium(IV), Halide Ions, and Photoreaction with Cerium(III). *Inorg. Chem.* **2009**, *48*, 1763−1773.

(9) Yao, Y.; Xu, C.; Yu, S.; Zhang, D.; Wang, S. Facile Synthesis of Mn_3O_4−Reduced Graphene Oxide Hybrids for Catalytic Decomposition of Aqueous Organics. *Ind. Eng. Chem. Res.* **2013**, *52*, 3637−3645.

(10) Shukla, P.; Sun, H.; Wang, S.; Ang, H. M.; Tadé, M. O. Nanosized Co_3O_4/SiO_2 for Heterogeneous Oxidation of Phenolic Contaminants in Waste Water. *Sep. Purif. Technol.* **2011**, *77*, 230−236.

(11) Anipsitakis, G. P.; Dionysiou, D. D.; Gonzalez, M. A. Cobalt-Mediated Activation of Peroxymonosulfate and Sulfate Radical Attack on Phenolic Compounds. Implications of Chloride Ions. *Environ. Sci. Technol.* **2005**, *40*, 1000−1007.

(12) Chen, X.; Chen, J.; Qiao, X.; Wang, D.; Cai, X. Performance of Nano-Co_3O_4/Peroxymonosulfate System: Kinetics and Mechanism Study Using Acid Orange 7 as a Model Compound. *Appl. Catal., B* **2008**, *80*, 116−121.

(13) Yang, Q.; Choi, H.; Al-Abed, S. R.; Dionysiou, D. D. Iron−Cobalt Mixed Oxide Nanocatalysts: Heterogeneous Peroxymonosulfate Activation, Cobalt Leaching, and Ferromagnetic Properties for Environmental Applications. *Appl. Catal., B* **2009**, *88*, 462−469.

(14) Saputra, E.; Muhammad, S.; Sun, H.; Ang, H. M.; Tadé, M. O.; Wang, S. Different Crystallographic One-dimensional MnO_2 Nanomaterials and Their Superior Performance in Catalytic Phenol Degradation. *Environ. Sci. Technol.* **2013**, *47*, 5882−5887.

(15) Xiao, W.; Wang, D.; Lou, X. W. Shape-Controlled Synthesis of MnO_2 Nanostructures with Enhanced Electrocatalytic Activity for Oxygen Reduction. *J. Phys. Chem. C* **2009**, *114*, 1694−1700.

(16) Hui, C.; Shen, C.; Tian, J.; Bao, L.; Ding, H.; Li, C.; Tian, Y.; Shi, X.; Gao, H.-J. Core-Shell Fe_3O_4@SiO_2 Nanoparticles Synthesized with Well-Dispersed Hydrophilic Fe_3O_4 Seeds. *Nanoscale* **2011**, *3*, 701−705.

(17) Yu, P.; Zhang, X.; Wang, D.; Wang, L.; Ma, Y. Shape-Controlled Synthesis of 3D Hierarchical MnO_2 Nanostructures for Electrochemical Supercapacitors. *Cryst. Growth Des.* **2008**, *9*, 528−533.

(18) Saputra, E.; Muhammad, S.; Sun, H.; Ang, H.-M.; Tadé, M. O.; Wang, S. Shape-Controlled Activation of Peroxymonosulfate by Single Crystal α-Mn_2O_3 for Catalytic Phenol Degradation in Aqueous Solution. *Appl. Catal., B* **2014**, *154*−*155*, 246−251.

(19) Sun, H. Q.; Ang, H. M.; Tade, M. O.; Wang, S. B. Co_3O_4 Nanocrystals with Predominantly Exposed Facets: Synthesis, Environmental and Energy Applications. *J. Mater. Chem. A* **2013**, *1*, 14427−14442.

(20) Balu, A. M.; Baruwati, B.; Serrano, E.; Cot, J.; Garcia-Martinez, J.; Varma, R. S.; Luque, R. Magnetically Separable Nanocomposites with Photocatalytic Activity under Visible Light for the Selective Transformation of Biomass-Derived Platform Molecules. *Green Chem.* **2011**, *13*, 2750−2758.

(21) Cano, M.; Sbargoud, K.; Allard, E.; Larpent, C. Magnetic Separation of Fatty Acids with Iron Oxide Nanoparticles and Application to Extractive Deacidification of Vegetable Oils. *Green Chem.* **2012**, *14*, 1786−1795.

(22) Zhang, L.; Qiao, S. Z.; Jin, Y. G.; Chen, Z. G.; Gu, H. C.; Lu, G. Q. Magnetic Hollow Spheres of Periodic Mesoporous Organosilica and Fe_3O_4 Nanocrystals: Fabrication and Structure Control. *Adv. Mater.* **2008**, *20*, 805−809.

(23) Liu, J.; Wang, B.; Budi Hartono, S.; Liu, T.; Kantharidis, P.; Middelberg, A. P. J.; Lu, G. Q.; He, L.; Qiao, S. Z. Magnetic Silica Spheres with Large Nanopores for Nucleic Acid Adsorption and Cellular Uptake. *Biomaterials* **2012**, *33*, 970−978.

(24) Yonghua, S.; Shizhang, Q.; Huagui, Y.; Chen, Y.; Yonggang, J.; Frances, S.; Jiayu, S.; Lina, C.; Changquan, L.; Gao Qing, L. Titanate−Silica Mesostructured Nanocables: Synthesis, Structural Analysis and Biomedical Applications. *Nanotechnology* **2010**, *21*, 065604.

(25) Wang, Y.; Sun, H.; Ang, H. M.; Tadé, M. O.; Wang, S. Magnetic Fe_3O_4/Carbon Sphere/Cobalt Composites for Catalytic Oxidation of Phenol Solutions with Sulfate Radicals. *Chem. Eng. J.* **2014**, *245*, 1−9.

(26) Wang, Y.; Sun, H.; Ang, H. M.; Tadé, M. O.; Wang, S. Synthesis of Magnetic Core/Shell Carbon Nanosphere Supported Manganese Catalysts for Oxidation of Organics in Water by Peroxymonosulfate. *J. Colloid Interface Sci.* **2014**, *433*, 68−75.

(27) Chandra, V.; Park, J.; Chun, Y.; Lee, J. W.; Hwang, I.-C.; Kim, K. S. Water-Dispersible Magnetite-Reduced Graphene Oxide Composites for Arsenic Removal. *ACS Nano* **2010**, *4*, 3979−3986.

(28) Guo, P.; Cui, L.; Wang, Y.; Lv, M.; Wang, B.; Zhao, X. S. Facile Synthesis of $ZnFe_2O_4$ Nanoparticles with Tunable Magnetic and Sensing Properties. *Langmuir* **2013**, *29*, 8997−9003.

(29) Zhang, S.; Li, J.; Zeng, M.; Zhao, G.; Xu, J.; Hu, W.; Wang, X. In Situ Synthesis of Water-Soluble Magnetic Graphitic Carbon Nitride Photocatalyst and Its Synergistic Catalytic Performance. *ACS Appl. Mater. Interfaces* **2013**, *5*, 12735−12743.

(30) Deng, H.; Li, X.; Peng, Q.; Wang, X.; Chen, J.; Li, Y. Monodisperse Magnetic Single-Crystal Ferrite Microspheres. *Angew. Chem., Int. Ed.* **2005**, *44*, 2782−2785.

(31) Jia, Z.; Ren, D.; Liang, Y.; Zhu, R. A New Strategy for the Preparation of Porous Zinc Ferrite Nanorods with Subsequently Light-Driven Photocatalytic Activity. *Mater. Lett.* **2011**, *65*, 3116−3119.

(32) Wang, M.; Ai, Z.; Zhang, L. Generalized Preparation of Porous Nanocrystalline $ZnFe_2O_4$ Superstructures from Zinc Ferrioxalate Precursor and Its Superparamagnetic Property. *J. Phys. Chem. C* **2008**, *112*, 13163−13170.

(33) Habibi, M. H.; Habibi, A. H.; Zendehdel, M.; Habibi, M. Dye-Sensitized Solar Cell Characteristics of Nanocomposite Zinc Ferrite Working Electrode: Effect of Composite Precursors and Titania as a Blocking Layer on Photovoltaic Performance. *Spectrochim. Acta, Part A* **2013**, *110*, 226−232.

(34) Tahir, A. A.; Wijayantha, K. G. U. Photoelectrochemical Water Splitting at Nanostructured $ZnFe_2O_4$ Electrodes. *J. Photochem. Photobiol., A* **2010**, *216*, 119−125.

(35) McDonald, K. J.; Choi, K.-S. Synthesis and Photoelectrochemical Properties of $Fe_2O_3/ZnFe_2O_4$ Composite Photoanodes for Use in Solar Water Oxidation. *Chem. Mater.* **2011**, *23*, 4863−4869.

(36) Aranishi, K.; Jiang, H.-L.; Akita, T.; Haruta, M.; Xu, Q. One-Step Synthesis of Magnetically Recyclable Au/Co/Fe Triple-Layered Core-Shell Nanoparticles as Highly Efficient Catalysts for the Hydrolytic Dehydrogenation of Ammonia Borane. *Nano Res.* **2011**, *4*, 1233−1241.

(37) Li, Z.; Ding, Y.; Xiong, Y.; Xie, Y. Rational Growth of Various α-MnO_2 Hierarchical Structures and β-MnO_2 Nanorods via a

Homogeneous Catalytic Route. *Cryst. Growth Des.* **2005**, *5*, 1953−1958.
(38) Li, Y.; Yi, R.; Yan, A.; Deng, L.; Zhou, K.; Liu, X. Facile Synthesis and Properties of $ZnFe_2O_4$ and $ZnFe_2O_4$/Polypyrrole Core-Shell Nanoparticles. *Solid State Sci.* **2009**, *11*, 1319−1324.
(39) Oaki, Y.; Imai, H. One-Pot Synthesis of Manganese Oxide Nanosheets in Aqueous Solution: Chelation-Mediated Parallel Control of Reaction and Morphology. *Angew. Chem., Int. Ed.* **2007**, *46*, 4951−4955.
(40) Portehault, D.; Cassaignon, S.; Nassif, N.; Baudrin, E.; Jolivet, J.-P. A Core−Corona Hierarchical Manganese Oxide and its Formation by an Aqueous Soft Chemistry Mechanism. *Angew. Chem., Int. Ed.* **2008**, *47*, 6441−6444.
(41) Wang, X.; Li, Y. Rational Synthesis of α-MnO_2 Single-Crystal Nanorods. *Chem. Commun.* **2002**, 764−765.
(42) Zhang, P.; Zhan, Y.; Cai, B.; Hao, C.; Wang, J.; Liu, C.; Meng, Z.; Yin, Z.; Chen, Q. Shape-Controlled Synthesis of Mn_3O_4 Nanocrystals and Their Catalysis of the Degradation of Methylene Blue. *Nano Res.* **2010**, *3*, 235−243.
(43) Yao, Y.; Cai, Y.; Lu, F.; Wei, F.; Wang, X.; Wang, S. Magnetic Recoverable $MnFe_2O_4$ and $MnFe_2O_4$-Graphene Hybrid as Heterogeneous Catalysts of Peroxymonosulfate Activation for Efficient Degradation of Aqueous Organic Pollutants. *J. Hazard. Mater.* **2014**, *270*, 61−70.
(44) Liang, H.; Sun, H.; Patel, A.; Shukla, P.; Zhu, Z. H.; Wang, S. Excellent Performance of Mesoporous Co_3O_4/MnO_2 Nanoparticles in Heterogeneous Activation of Peroxymonosulfate for Phenol Degradation in Aqueous Solutions. *Appl. Catal., B* **2012**, *127*, 330−335.
(45) Sun, H.; Wang, Y.; Liu, S.; Ge, L.; Wang, L.; Zhu, Z.; Wang, S. Facile Synthesis of Nitrogen Doped Reduced Graphene Oxide as a Superior Metal-Free Catalyst for Oxidation. *Chem. Commun.* **2013**, *49*, 9914−9916.
(46) Saputra, E.; Muhammad, S.; Sun, H.; Ang, H.-M.; Tadé, M. O.; Wang, S. Manganese Oxides at Different Oxidation States for Heterogeneous Activation of Peroxymonosulfate for Phenol Degradation in Aqueous Solutions. *Appl. Catal., B* **2013**, *142−143*, 729−735.
(47) Anipsitakis, G. P.; Dionysiou, D. D. Degradation of Organic Contaminants in Water with Sulfate Radicals Generated by the Conjunction of Peroxymonosulfate with Cobalt. *Environ. Sci. Technol.* **2003**, *37*, 4790−4797.
(48) Neta, P.; Huie, R. E.; Ross, A. B. Rate Constants for Reactions of Inorganic Radicals in Aqueous Solution. *J. Phys. Chem. Ref. Data* **1988**, *17*, 1027−1284.
(49) Rosen, G. M.; Rauckman, E. J. Spin Trapping of the Primary Radical Involved in the Activation of the Carcinogen N-Hydroxy-2-acetylaminofluorene by Cumene Hydroperoxide-Hematin. *Mol. Pharmacol.* **1980**, *17*, 233−238.
(50) Floyd, R. A.; Soong, L. M. Spin Trapping in Biological Systems. Oxidation of the Spin Trap 5,5-Dimethyl-1-pyrroline-1-oxide by a Hydroperoxide−Hematin−System. *Biochem. Biophys. Res. Commun.* **1977**, *74*, 79−84.
(51) Fang, G.-D.; Dionysiou, D. D.; Al-Abed, S. R.; Zhou, D.-M. Superoxide Radical Driving the Activation of Persulfate by Magnetite Nanoparticles: Implications for the Degradation of PCBs. *Appl. Catal., B* **2013**, *129*, 325−332.
(52) Huang, Y.-F.; Huang, Y.-H. Behavioral Evidence of the Dominant Radicals and Intermediates Involved in Bisphenol A Degradation Using an Efficient Co^{2+}/PMS Oxidation Process. *J. Hazard. Mater.* **2009**, *167*, 418−426.
(53) Buxton, G. V.; Greenstock, C. L.; Helman, W. P.; Ross, A. B. Critical Review of Rate Constants for Reactions of Hydrated Electrons, Hydrogen Atoms and Hydroxyl Radicals (OH/O^-) in Aqueous Solution. *J. Phys. Chem. Ref. Data* **1988**, *17*, 513−886.